2 Detector and physics performance

Disclaimer: This is a very preliminary draft. Work is still ongoing. Checks on the validity of the samples generated are ongoing. Exclusive dijet analysis results are not yet presented.

The PPS forward proton measurement capability will enhance the ability of the CMS detector to carry out the primary physics program of the LHC in various sectors and extensions of the SM. The PPS detector consists of a series of Roman Pot (RP) stations capable of performing precision position and time-of-flight measurements of the leading protons coming from the Interaction Point (IP). Studies include QCD processes in the exclusive dijet final states through gluon-guon interaction, as well as electroweak physics in two-photon interactions. Discussion of the performance of the PPS tracking and timing detectors is presented, with the goal of estimating the sensitivity reach during the Run 2 data-taking period.

A brief description of the beam optics is provided in Sec. 2.1, details of the simulated samples are given in Sec. 2.2, detector acceptance and resolution are presented in Sec. 2.3 and Sec. 2.4. The extrapolation of the machine-induced background is described in Sec. 2.6, and the RP alignment in Sec. 2.7. Finally, measurements and sensitivity reach for two reference physics processes are discussed in Sec. 2.8.

2.1 Beam optics

The proposed forward detector tracking and timing detector stations are to be installed in the regions located at approximately z=204 m and z=215 m from the IP, in both beam directions downstream of the central detector. Protons that have lost energy in the primary interaction emerge laterally after passing through the bending magnets. At z=204-215 m one can detect protons that have lost a few percent ($\simeq 3 - 10\%$) of the initial beam energy.

The trajectory of protons produced with transverse position* (x^*, y^*) and angle (Θ_x^*, Θ_y^*) at the IP5 location is described by the equation

$$\vec{d} = T \cdot \vec{d}^* \,, \tag{2.1}$$

where $\vec{d} = (x, \Theta_x, y, \Theta_y, \Delta p/p)^T$ and T is the transport matrix; p and Δp denote the nominal beam momentum and the proton longitudinal momentum loss, respectively. The transport matrix is defined as:

$$T = \begin{pmatrix} v_x & L_x & m_{13} & m_{14} & D_x \\ \frac{dv_x}{ds} & \frac{dL_x}{ds} & m_{23} & m_{24} & \frac{dD_x}{ds} \\ m_{31} & m_{32} & v_y & L_y & D_y \\ m_{41} & m_{42} & \frac{dv_y}{ds} & \frac{dL_y}{ds} & \frac{dD_y}{ds} \\ 0 & 0 & 0 & 0 & 1 \end{pmatrix} \tag{2.2}$$

where the magnification $v_{x,y} = \sqrt{\beta_{x,y}/\beta^*} \cos \Delta\phi_{x,y}$, and the effective length $L_{x,y} = \sqrt{\beta_{x,y}\beta^*} \sin \Delta\phi_{x,y}$ are functions of the betatron amplitude $\beta_{x,y}$ and the relative phase advance up to the RP location $\Delta\phi_{x,y} = \int_{IP}^{RP} \frac{ds}{\beta(s)_{x,y}}$. Together with the dispersion $D_{x,y}$ (where nominally $D_y = 0$), they are of particular importance for the reconstruction of the proton kinematics.

Figure 1 shows the values of the effective lengths in X and Y (L_x and L_y) and the corresponding dispersions (D_x and D_y) as a function of $\xi = \Delta p/p$ (momentum loss of the surviving proton) at the detector location at z=204 m. These values, together with the beam widths and divergences, determine acceptance and resolution in the proton kinematic variables t (four-momentum transfer) and ξ. In the proton transport, no uncertainty in the optical function is assumed in the reconstruction of the kinematical vari-

---

The '' superscript indicates the LHC Interaction Point 5 (IP5).

ables. The optical functions will be determined based on the real beam optics, and their resolution will be estimated according to the method used in Ref. [47].
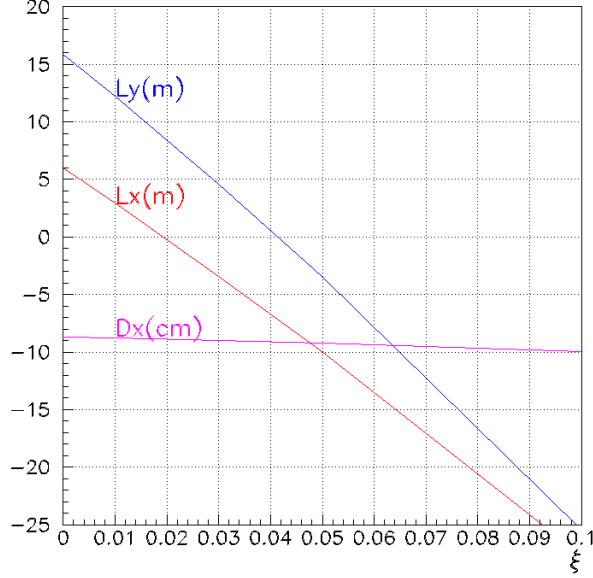

Figure 1: FIXME: USE PDF Effective lengths in X and Y (L_x and L_y), and the corresponding dispersion (D_x) as a function of the proton momentum loss ξ at z=204 m from the interaction point.

The configuration of the LHC beamline around the CMS interaction point is shown in Fig. 2 for the positive side (z>0). Particle transport from the interaction region IP5 to the PPS detector location is performed with HECTOR [40], which is incorporated in the CMSSW detector simulation and reconstruction package. Results are found in good agreement with MAD-X [41], the standard LHC beam transport program used at CERN. The HECTOR package tracks protons (or other particles) that emerge in the forward direction from the interaction region through the LHC beam pipes. The model of the LHC beamline is implemented, and the collimators and the apertures of the beamline elements are taken into account. The beam transport can be updated for different optics configurations.

In these studies, a proton beam energy of 6.5 TeV with the LHC standard optics files (v6.5) is used. The beam size can be expressed by the emittance ϵ, and the amplitude function β. The horizontal beam size in the range of the PPS detector location is shown in Fig. 3. The emittance is inversely proportional to the beam momentum; increasing the momentum of the beam reduces the emittance and hence the physical size of the beam Therefore, the normalized emittance $\epsilon_n = \epsilon \cdot \beta \cdot \gamma$ (where β, γ are the relativistic functions) is often used instead. Values for the amplitude function at the IP $\beta^* = 0.6$m, normalized emittance, $\epsilon_n \simeq 3.75 \cdot 10^{-6}$m (emittance $\epsilon \simeq 5.4 \cdot 10^{-10}$m) and crossing angle of 142.5μrad in the horizontal plane are used. Position of the forward protons depends on the beam optics; vertex smearing of $\sigma_{x,y} = 15\mu$m and angular beam divergence of $\sigma_\theta = 30\mu$rad at the IP, are used.

2.2 Detector simulation

In order to study the detector occupancy and acceptance for a given physics process, dedicated samples of exclusive dijet and WW events are used, produced in gluon-gluon fusion and photon-photon interactions, respectively. Here (and in the following), the term "exclusive" refers to the production of a particular process (in this case, dijets or WW) without "anything else" coming from the primary hard interaction. In the absence of additional interactions, large "rapidity gaps", i.e. regions in pseudorapidity devoid of particle production, are expected around the exclusively centrally produced system. In both cases, the central systems of dijets or WW are required to be produced with rapidity $|y| < 2$, in proton-proton
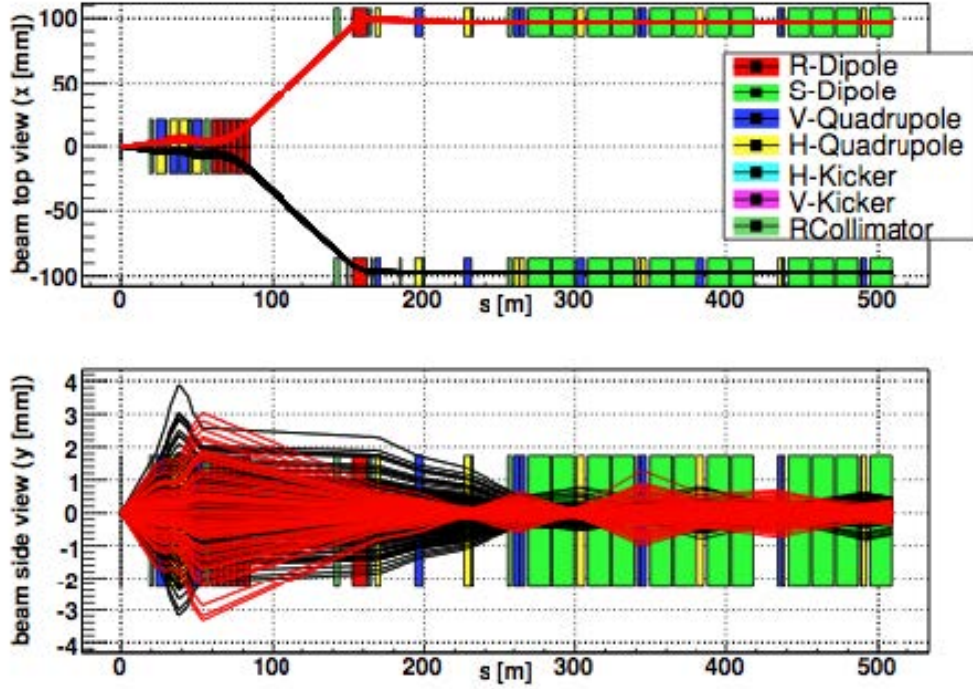
Figure 2: Top (*top*) and side (*bottom*) views of the beamline on the positive side (z>0) of IP showing the proton trajectories using HECTOR, a fast simulator for particle transport in the beamline. The black (red) lines correspond to the particles going into (out of) the IP. Here, the horizontal curvature of the beamline has been straightened out for the purpose of simplification.

collisions at $\sqrt{s} = 13$ TeV. The signal events are generated with ExHuME [43] to simulate exclusive dijet events, while the FPMC generator [42] is used to simulate exclusive WW events from the process $pp \rightarrow pWWp$. Both in the exclusive dijet and WW samples, events are generated in the $|t|$ and ξ ranges corresponding to $0 < |t| < 4, 0.01 < \xi < 0.2$. Beam energy dispersion and crossing angle including the smearing due to the beam divergence, vertex smearing, and detector resolution effects are accounted for. The presence of multiple interactions (pileup) per bunch crossing is incorporated by simulating additional interactions (both in-time and out-of- time with the collision) with a multiplicity of $\mu = 50$ matching that expected during Run 2. PYTHIA is used to generate the pileup events from minimum bias (see Sec. 2.5).

2.3 Detector acceptance and resolution: ξ, t

add some details on the fast detector simulation (geometry, etc).

The dimensions of the PPS detectors (both timing and tracking) are constrained by the allocated space in the RP, and eventually determine the coverage in t, ξ. Particles with fixed values of $(|t|, \xi)$ propagated to the PPS detector location arrive at the X,Y positions shown in Fig. 4. They form ellipses due to the quadrupole magnets, with centers at $y = 0$. From Fig. 4 one can estimate the acceptance for any detector coverage for a given t, ξ, as the fraction of the corresponding ellipse covered. The rectangle drawn by a dashed (solid) black line illustrates the boundaries of a detector with an area (in X, Y) of 20×18 mm^2 located at 15σ (20σ)+0.3 mm from the beam center, whereas the beam envelopes are schematically drawn by ellipses centered at zero. The additional 0.3 mm account for the thin RP window separating the active detectors from the beam vacuum.

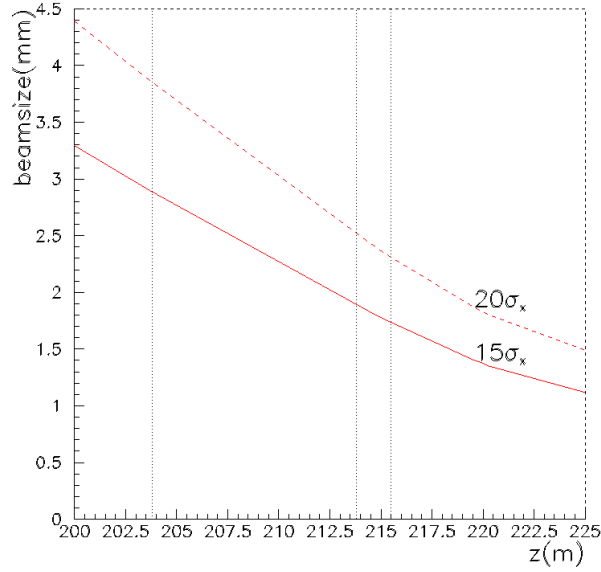The particle hit distribution is studied for dimensions of the active area of the tracking stations at z=204 m

Figure 3: FIXME: USE PDF Horizontal beam size in the z range location corresponding to the tracking and timing detector stations.

and z=215 m, where detector planes are orthogonal to the beam direction. Detector segmentation is not implemented in the simulation, as tracking detectors are expected to have a finely segmented active area (pixel size in X,Y is $\approx 100 \times 150\ \mu\text{m}^2$). The corresponding resolution of FIXME xx μm is assumed in the smearing of the proton reconstruction position.

Figure 5 shows the hit distributions in the tracking detectors at z=204 m for exclusive dijet (left) and WW (right) events. The black squared lines schematically illustrate the X and Y dimensions ($20 \times 18\ \text{mm}^2$) FIXME: CHECK DIMENSIONS of the detectors when placed at 15σ from the beam center. Detector and beam resolution effects are included in these plots.

The acceptance is estimated for a distance of the tracking detectors of 15σ and 20σ from the beam center. Here and in the following, a "dead" space of 0.3 mm is added to the 15σ (or 20σ) "distance", to account for the distance between the RP window and the active detector area.

Figure 6 shows the single-arm acceptance in the two-dimensional $(\xi, |t|)$ plane, when hits are required in both tracking stations (at z=204 m and z=215 m). The acceptance is estimated using a sample of exclusive dijet events produced with the ExHuME signal generator, when the tracking detectors are placed at 15σ (left) and 20σ (right) from the beam center. A track reconstruction efficiency of 100% is assumed. The loss of track efficiency due to proton interaction with the RP window is estimated to be 1-2% [44].

For exclusive dijet events, an acceptance of approximately 49% is estimated (at 15σ) when the protons are within the PPS detector geometrical acceptance. Acceptance values are estimated with respect to the cross section of the generated events ($0 < |t| < 4, 0.01 < \xi < 0.2$). Similar two-dimensional acceptance distributions in the $(\xi, |t|)$ plane are shown in Fig. 7 for a double-arm acceptance, i.e. when hits in the tracking stations on both sides of the IP are required. An acceptance of approximately 11% is estimated when the protons are within the PPS detector geometrical acceptance.

Single-arm and double-arm hit distributions in the $(\xi, |t|)$ plane for exclusive WW events produced with the FPMC signal generator are shown in Fig. 8 and Fig. 9, respectively. Distributions are shown for a distance of the tracking detectors at 15σ (left) and 20σ (right) from the beam center. A single-arm (double-arm) acceptance of approximately 57% (30%) is estimated when the protons are within the PPS detector geometrical acceptance.

The full set of kinematic variables is reconstructed with the use of Eq. 2.1. The scattering angle res-
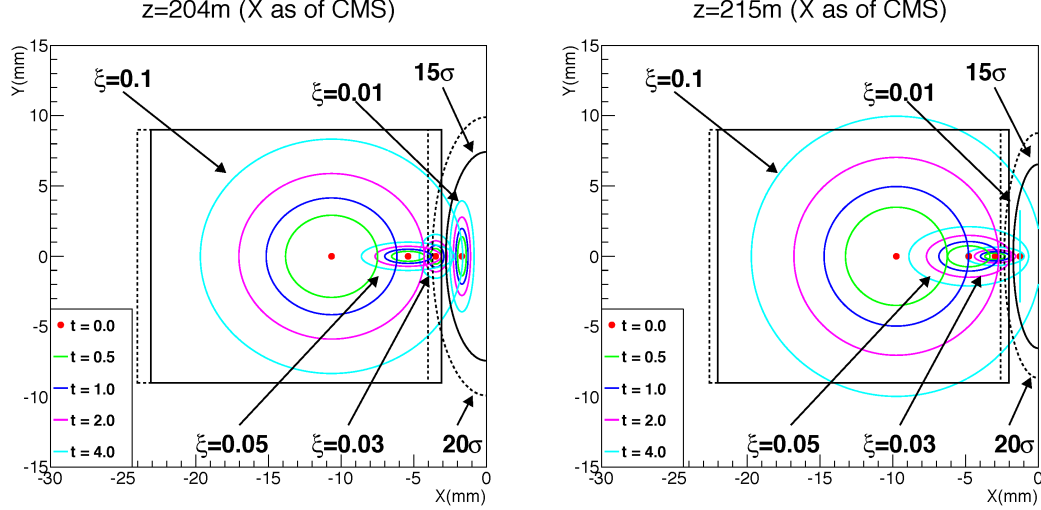
Figure 4: Particles with fixed t and ξ values propagated to the PPS detector position: $t - \xi$ ellipses for the protons at z=204 m (left) and z=215 m (right). The solid (dashed) black rectangle illustrates the detector dimensions at 15σ (20σ) from the beam center. The beam dimensions are also shown by circles. A "particle-gun" simulation based on HECTOR is used to generate protons at different (t, ξ, ϕ) values.

olution depends mainly on the angular beam divergence and on the detector resolution. As the values of the optical function parameters vary with the proton momentum loss, this will result in ξ-dependent resolution for the main variables $\Theta^*_{x,y}$ and ξ. Moreover, as a dispersion term is present in the horizontal projection (cf. Eq. 2.1), both Θ^*_x and ξ contribute in determining the horizontal trajectory, thus resulting in a correlation of these two variables.

Generated and reconstructed values of t and ξ are compared in Fig. 10 and Fig. 11, respectively. The distributions are shown for the sample of exclusive dijet events. A linear correlation is found between the generated and reconstructed values over the entire range ($0 < |t| < 4, 0.03 < \xi < 0.2$). The resolution, i.e. the discrepancy of the reconstructed from the generated t and ξ values, is shown after accounting for the full smearing of the measurement.

Similar t and ξ distributions for exclusive WW events are shown in Fig. 13 and Fig. 14, respectively.

2.4 Detector acceptance and resolution: mass

The mass acceptance and the achievable experimental resolution of the forward detectors depends ultimately on the LHC beam optics and on the position of the PPS detectors relative to the beam.

The acceptance as a function of the mass of a central system produced is shown in Fig. 15. Central exclusive dijet (left) or WW (right) events are studied. With detectors at 15σ from the beam, the PPS selects exclusive systems with masses in the 400-1700 GeV range, with an acceptance of at least 10%. The lower mass reach is strongly dependent on the distance of closest approach of the detectors. In general, both stations have larger acceptance for central systems in photon-photon than in gluon-gluon interactions (because of the smaller $|t|$). The distributions also show that the acceptance varies substantially with the distance of the tracking detectors from the beam. Operation of the detectors at 15σ (dashed lines in the plot) increases the acceptance for masses in the range of 400-1000 GeV. Beam energy dispersion and crossing angle at the IP, and detector resolution effects are included in the estimate of the acceptance.

The mass is reconstructed with a resolution of approximately 2-3% from the generated mass of the produced system. The expected reconstructed mass resolution for the entire mass system range studied ($0.3 < M_X < 2$ TeV) is shown in Fig. 16. Figure 17 shows the mass resolution estimated as a function
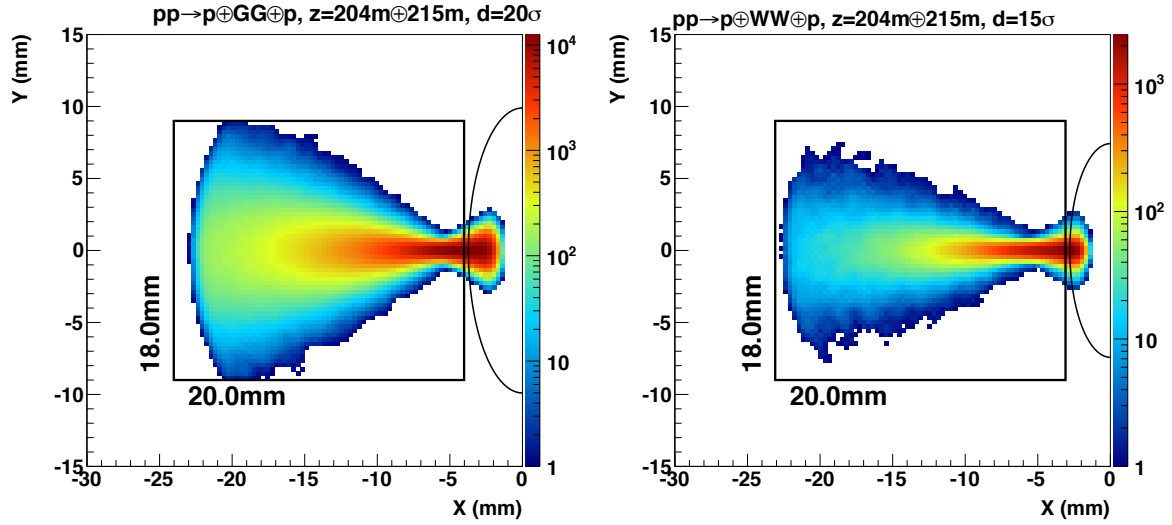
Figure 5: FIXME: HERE AND ELSEWHERE, TITLE REPLACE "GG" WITH "JJ" Hit distributions for centrally produced exclusive dijet (left) and WW (right) events are shown for the tracking detectors located at z=204 m. The black squared line schematically illustrates the boundaries of the tracking detectors in X and Y, when located at 15σ from the beam center (circle line). Beam energy and vertex smearing, and detector resolution are accounted for.

of the mass of the centrally produced events in exclusive dijet (left) and WW (right) events.

2.4.1 Timing Detectors

Occupancy of the time-of-flight detectors are studied for different detector geometries. Occupancy studies are performed for both dijet (Fig. 18) and WW (Fig. 19) exclusive events, where 50 pileup interactions are superimposed on the primary interaction. Smearing effects due to vertex position, beam energy dispersion and crossing angle are accounted for. Segmentation of the timing detector active area is considered for both the baseline option of the QUARTIC detectors, and for the study-option of "diamond-like" detectors. The QUARTIC geometry is constrained by the minimal transversal dimensions (due to the machining of the detector bars) and by the outgoing proton direction/angle, as each particle must be contained within the same detector bar in order to maximize the signal yield and minimize the cross-talk between neighboring bars. The latter is not a limiting factor as, at the PPS location, the deflection in x per mm travelled in z is small, and it is approximately $\Delta x(\text{per mm}) \simeq 0.02 - 0.06$ μm. On the other hand, the "diamond-like" detector segmentation offers a flexible geometry by allowing the optimization of the detector occupancy depending on the distance from the beam center, thus reducing the occupancy rates closer to the beam. In the simulation, each L-shaped QUARTIC bar has the same X-Y transversal section of 3×3 mm^2; the "diamond-like" cells have a Y-dimension of 5 mm, with a variable width (in X) varying from 0.3 mm (closer) up to 4.6 mm (further away) depending on the distance from the beam. Multiple hits in the same cell "blinds" the detector functionality, and therefore –when this happens– the time-of-flight information cannot be used for rejecting pileup events. Such events are not used in the data analysis, thus causing a source of inefficiency.
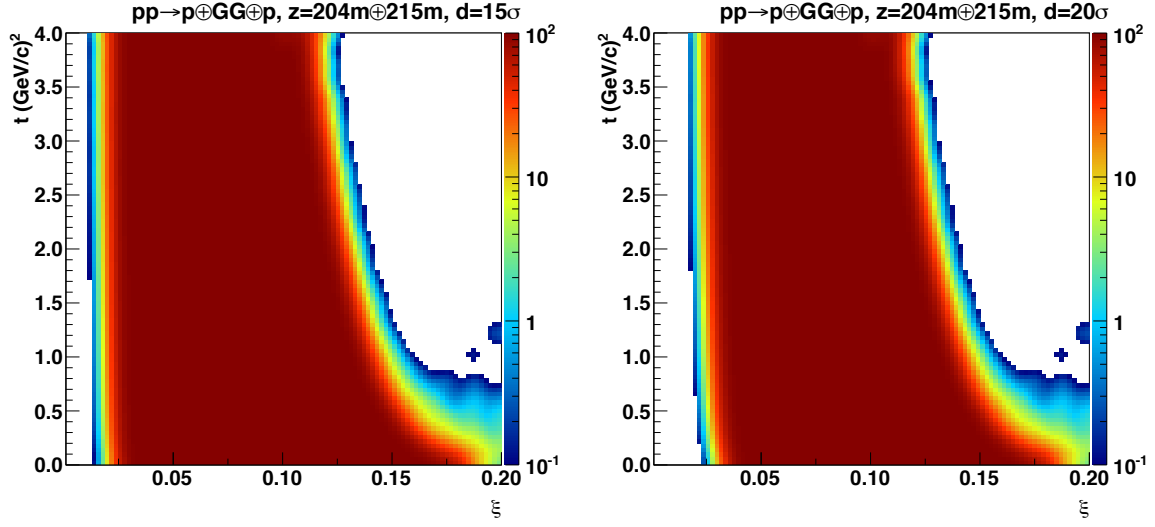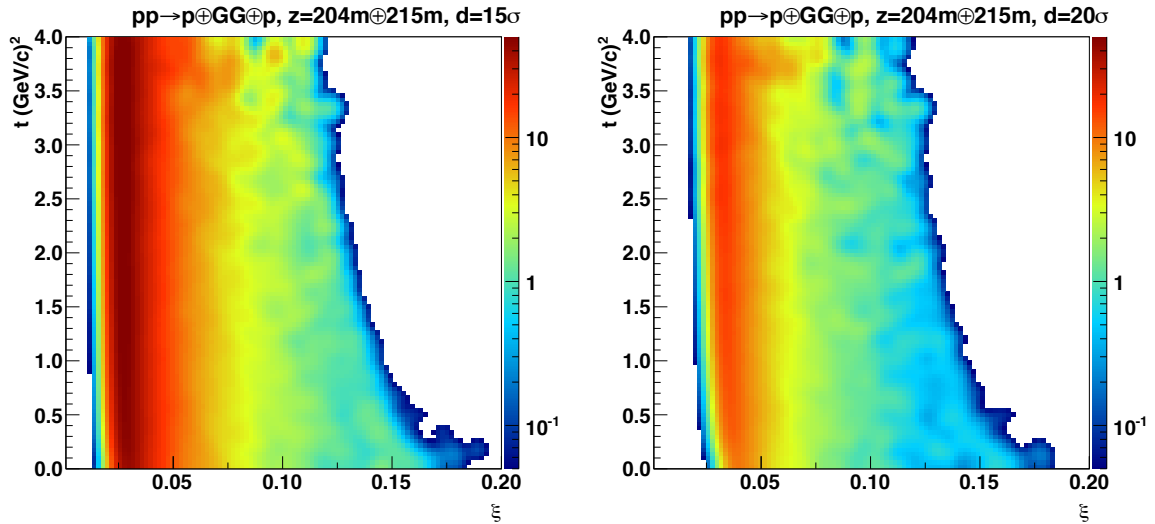
2.5 Background: pile-up

add discussion of pileup

Figure 6: Acceptance in the $(\xi, |t|)$ plane for events in a single PPS arm, when requiring the coincidence of hits in the tracking stations at z=204 m and z=215 m only on one side of the IP. The ExHuME signal generator is used to simulate exclusive dijet events. The acceptance is shown for a distance of the tracking detectors at 15σ (left) and 20σ (right) from the beam center. Pileup events are not included.

Figure 7: Acceptance in the $(\xi, |t|)$ plane for events in a single PPS arm, when requiring the coincidence of hits in the tracking stations at z=204 m and z=215 m on both sides of the IP. The ExHuME signal generator is used to simulate exclusive dijet events. The acceptance is shown for a distance of the tracking detectors at 15σ (left) and 20σ (right) from the beam center. Pileup events are not included.
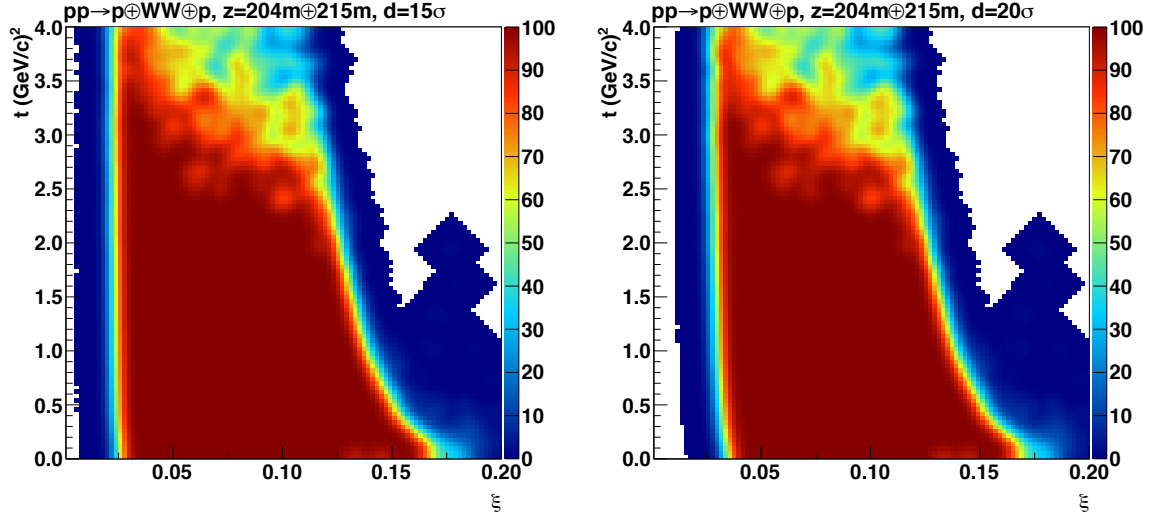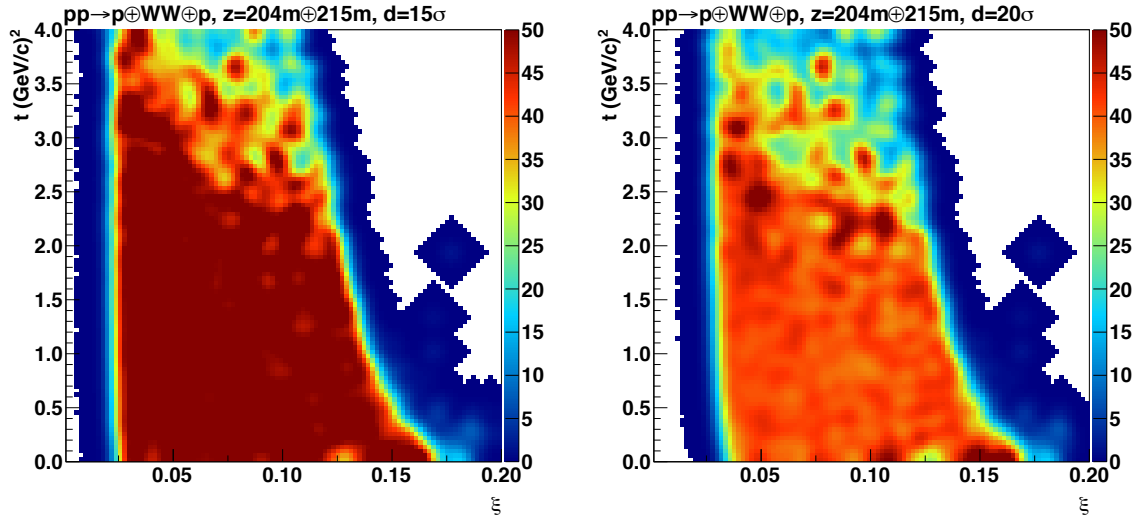
Figure 8: **FIXME: Z AXIS IN LOG SCALE** Acceptance in the $(\xi, |t|)$ plane for events in a single PPS arm, when requiring the coincidence of hits in the tracking stations at z=204 m and z=215 m only on one side of the IP. The FPMC signal generator is used to simulate $pp \rightarrow pWWp$ exclusive events. The acceptance is shown for a distance of the tracking detectors at 15σ (left) and 20σ (right) from the beam center. Pileup events are not included.

Figure 9: **FIXME: Z AXIS IN LOG SCALE** Acceptance in the $(\xi, |t|)$ plane for events selected in a double PPS arm, i.e. when requiring the coincidence of hits in the tracking stations at z=204 m and z=215 m on both sides of the IP. The FPMC signal generator is used to simulate $pp \rightarrow pWWp$ exclusive events. The acceptance is shown for a distance of the tracking detectors at 15σ (left) and 20σ (right) from the beam center. Pileup events are not included.
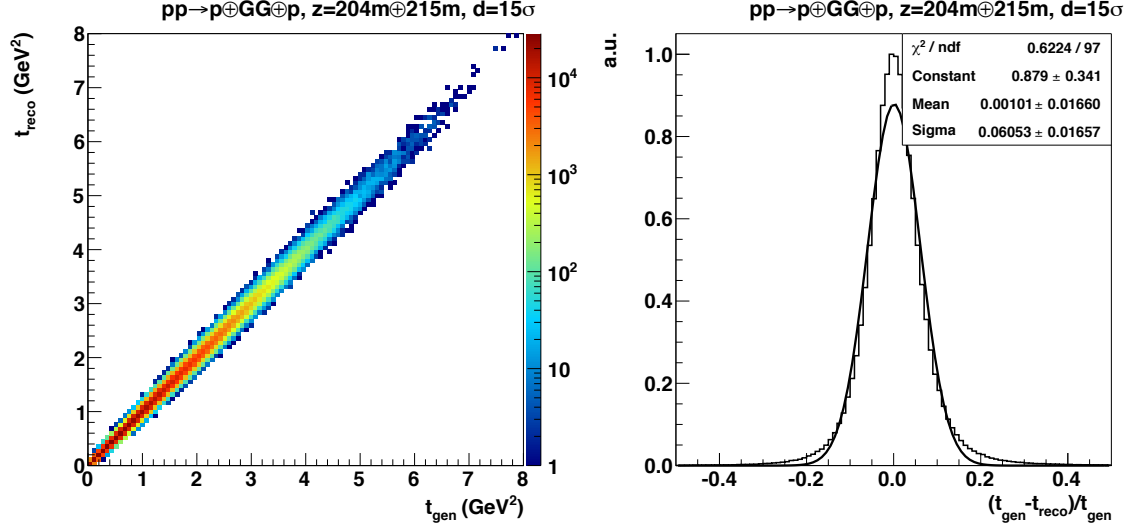
Figure 10: *Left:* Generated vs. reconstructed value of t for the protons within the PPS detector acceptance ($0 < |t| < 4, 0.01 < \xi < 0.2$). In the reconstruction, smearing effects due to vertex position, beam energy dispersion and crossing angle are accounted for. *Right:* Resolution of the reconstructed t measurement, $(t_{reco} - t_{gen})/t_{gen}$. The ExHuME signal generator is used to simulate exclusive dijet events. The acceptance is shown for a distance of the tracking detectors at 15σ from the beam center.
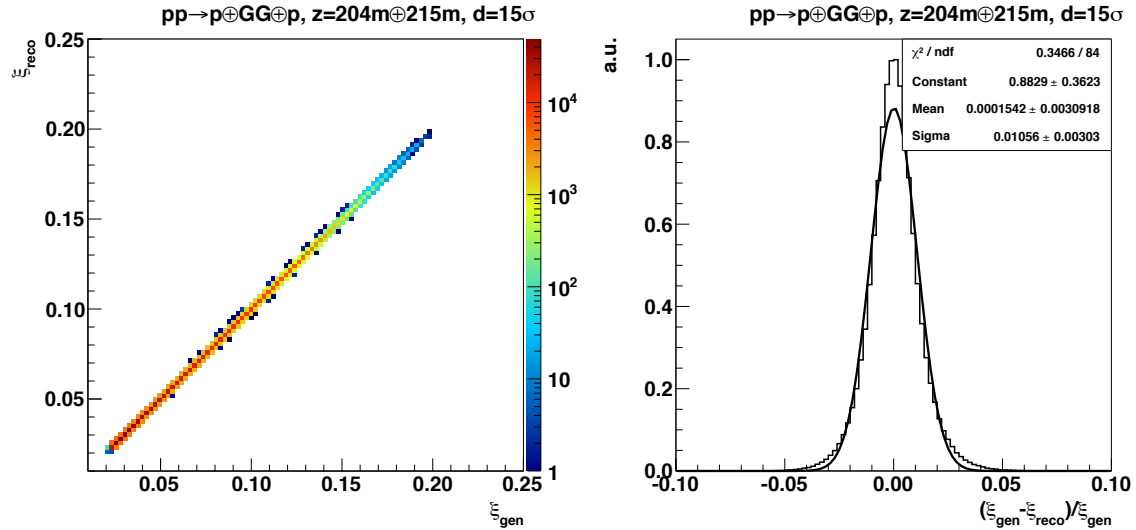

Figure 11: *Left:* Generated vs. reconstructed value of ξ for the protons within the PPS detector acceptance ($0 < |t| < 4, 0.01 < \xi < 0.2$). In the reconstruction, smearing effects due to vertex position, beam energy dispersion and crossing angle are accounted for. *Right:* Resolution of the reconstructed ξ measurement, $(\xi_{reco} - \xi_{gen})/\xi_{gen}$. The ExHuME signal generator is used to simulate exclusive dijet events. The acceptance is shown for a distance of the tracking detectors at 15σ from the beam center.
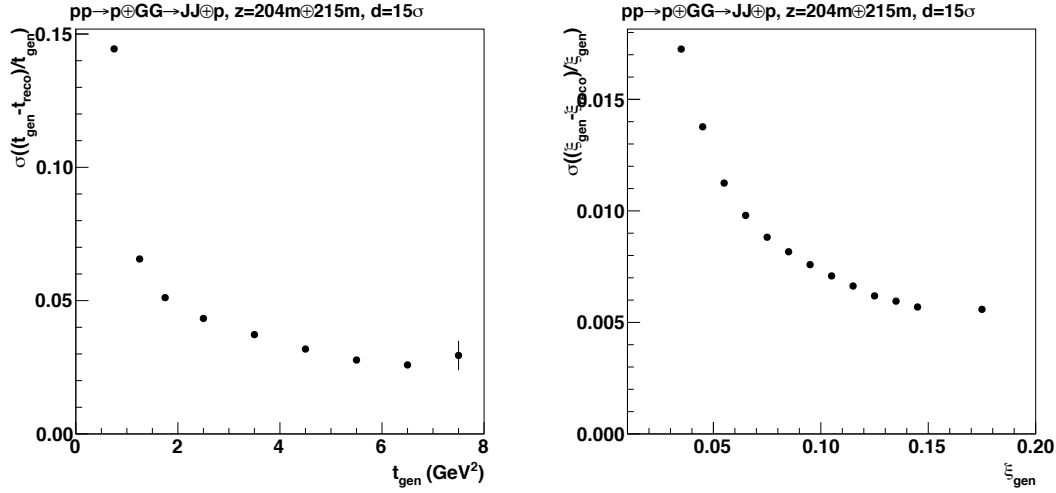
Figure 12: Resolution of the reconstructed t (left) and ξ (right) measurements, $(t_{reco} - t_{gen})/t_{gen}$ $((\xi_{reco} - \xi_{gen})/\xi_{gen})$ as a function of the generated values, t_{gen} and ξ_{gen}, respectively. In the reconstruction, smearing effects due to vertex position, beam energy dispersion and crossing angle are accounted for. The ExHuME signal generator is used to simulate exclusive dijet events. The acceptance is shown for a distance of the tracking detectors at 15σ from the beam center.

2.6 Background : pp induced background

In addition to the genuine physics processes from the hard interaction or from pileup events, instrumental background due to beam-gas interaction or any other "machine-induced" background must be estimated.

The machine-induced background contribution at z=204-215 m is estimated by extrapolating the measurements by the TOTEM Roman Pot detectors, in the same location and with real data during the 2010-2012 proton-proton run, to the new beam intensity and data-taking conditions expected for Run 2.

Different approaches have been used to understand how to extract the background component from the data and how to extrapolate it to higher pile-up conditions. The detailed procedure is described in [45]. Briefly, it can be summarized as in the following: the background probability per bunch-crossing is estimated directly using a zero-bias data sample. A MC simulation estimates the multiplicity of the primary tracks reconstructed in the horizontal pots. By comparing the primary multiplicity with the inclusive cluster multiplicity from the data it is then possible to extract the probability of the background multiplicity per bunch-crossing. These results are used to extract the scale factors to be applied to a simulation with $\mu = 50$, and extrapolate the tracking multiplicity due to machine-induced backgrounds expected for Run 2 conditions. The cluster multiplicity at μ=50 is shown in Fig. 20.

2.7 Roman Pot detector alignment

The values of both ξ and t can be accurately determined from PPS reconstructed track coordinates and the position of the event vertex at the interaction point using the beam-transport matrix between the interaction point and the PPS. Crucial for this determination is the detector X-Y alignment with respect to the beam. The alignment procedure must be repeated for each data-taking period.

Precise knowledge of the position of the detector with respect to the circulating beam at the moment of the measurement (order of μm) is needed for physics performance and, since one desires to approach the beam as closely as possible, a delicate procedure must be repeated for each run.

The alignment process is composed of three steps applied in sequence: 1) absolute alignment of the
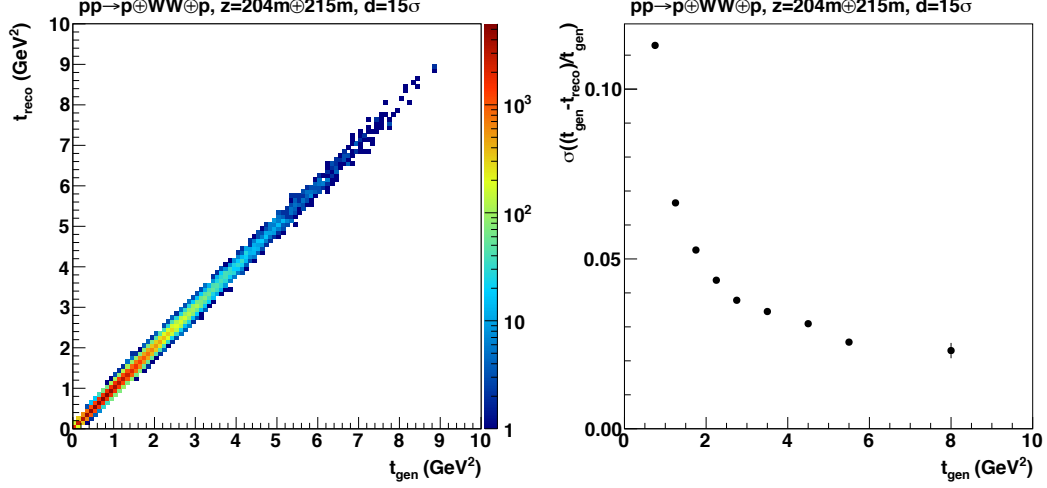
19

Figure 13: *Left:* Generated vs. reconstructed value of t for the protons within the PPS detector acceptance ($0 < |t| < 4, 0.01 < \xi < 0.2$). In the reconstruction, smearing effects due to vertex position, beam energy dispersion and crossing angle are accounted for. *Right:* Resolution of the reconstructed t measurement, $(t_{reco} - t_{gen})/t_{gen}$ as a function of the generated value t_{gen}. The FPMC signal generator is used to simulate exclusive WW events. The acceptance is shown for a distance of the tracking detectors at 15σ from the beam center.
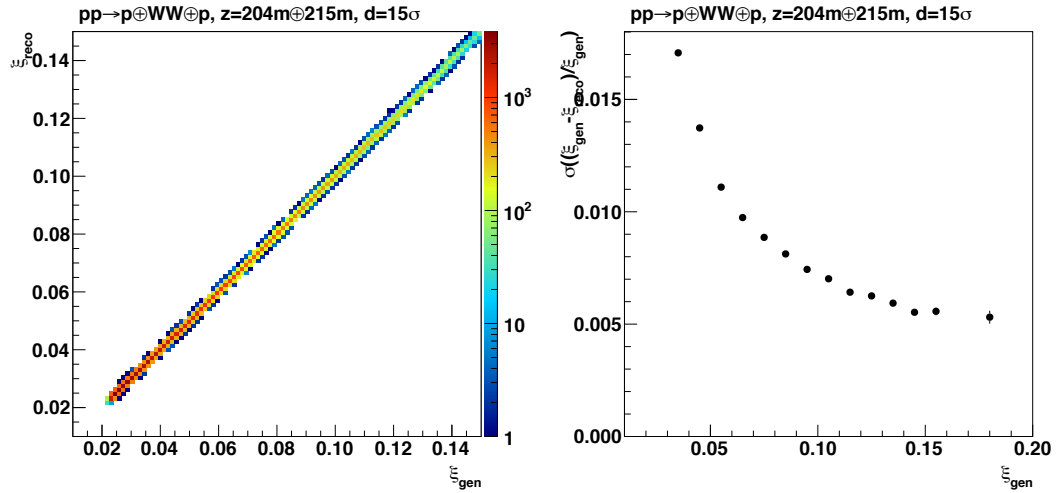

Figure 14: *Left:* Generated vs. reconstructed value of ξ for the protons within the PPS detector acceptance ($0 < |t| < 4, 0.01 < \xi < 0.2$). In the reconstruction, smearing effects due to vertex position, beam energy dispersion and crossing angle are accounted for. *Right:* Resolution of the reconstructed ξ measurement, $(\xi_{reco} - \xi_{gen})/\xi_{gen}$ as a function of the generated value ξ_{gen} The FPMC signal generator is used to simulate exclusive WW events. The acceptance is shown for a distance of the tracking detectors at 15σ from the beam center.
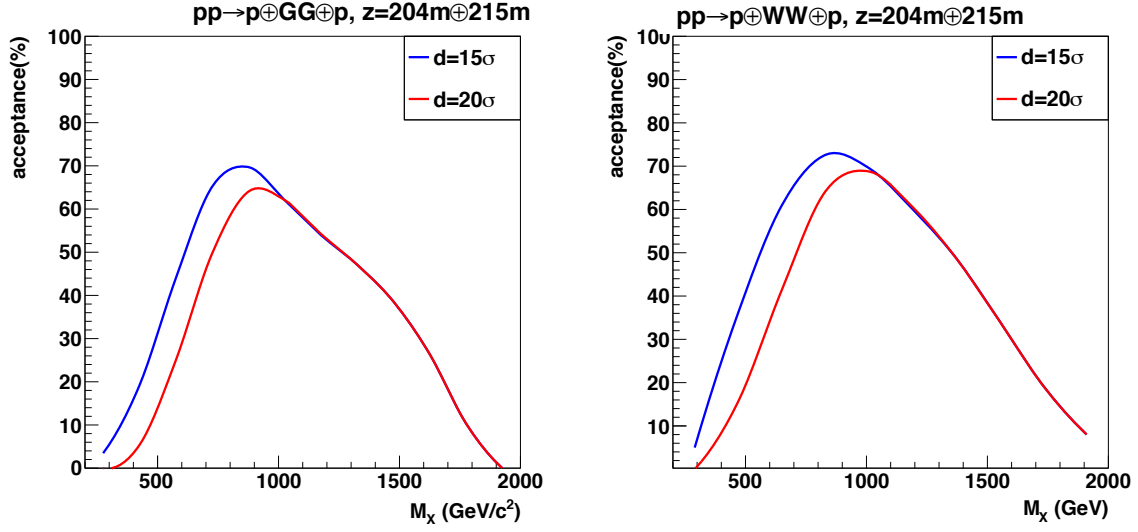
Figure 15: FIXME: HERE AND ANYWHERE, USE C=1 Mass acceptance as a function of centrally produced mass for exclusive diet events produced in gluon fusion (left, computed with ExHuME), and exclusive WW events produced in photon-photon processes (right, computed with FPMC). In the simulation, a coincidence of the tracking detectors placed at z=204 m and z=215 m is required. The estimated acceptance is shown as a solid (dashed) line when the tracking detectors are located at a distance of 15 (20) σ from the beam center.
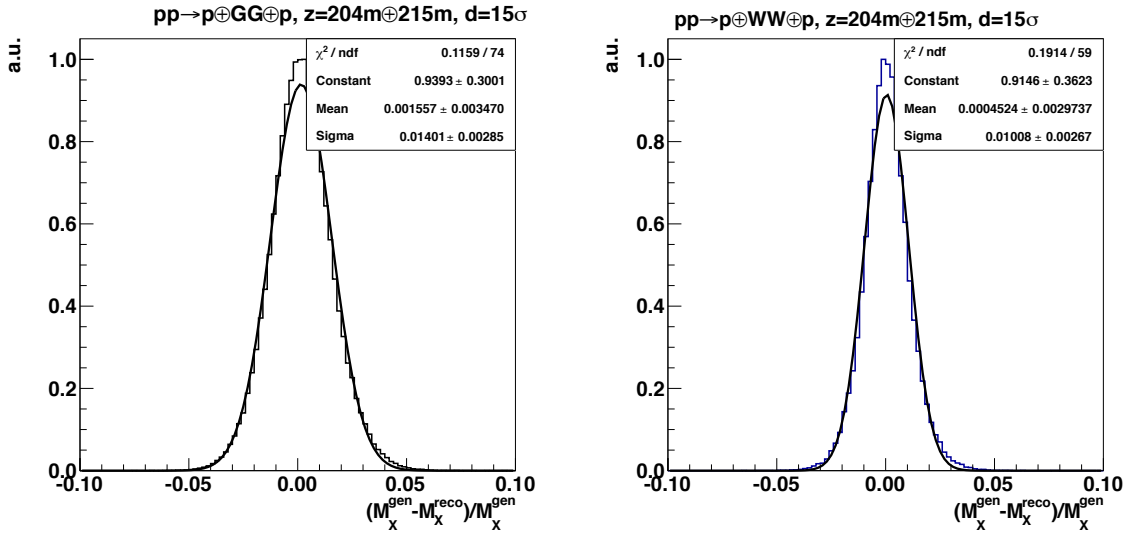

Figure 16: Reconstructed mass resolution for centrally produced events in the entire mass system range studied ($0.3 < M_X < 2$ TeV), in exclusive dijet (left) and in WW (right) events. The estimated resolution is shown for tracking detectors located at a distance of 15 σ from the beam center.
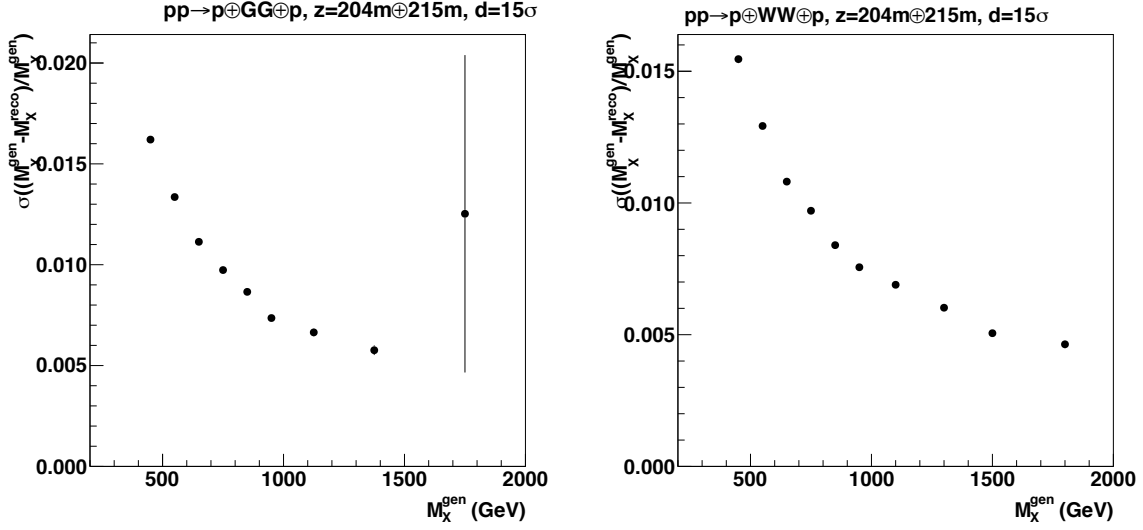
21

Figure 17: Mass resolution as a function of the mass M_X of the centrally produced events in exclusive dijet (left) and WW (right) events. The estimated resolution is shown for tracking detectors located at a distance of 15 σ from the beam center.

detector RP housing position with respect to the beam, 2) relative alignment of the individual RP detector position with respect to each other, and 3) global alignment of detectors in different RPs (performed using elastic events). These steps are described in the following.

1. Alignment between the RP and the circulating beam: A special fill is required to determine the position of the RPs and their detectors (alignment) with respect to the circulating beam with a procedure similar to the one employed for the LHC collimators. The precision of this procedure is determined by the RP movement in steps varying between 10 μm and 50 μm. Due to a poorly defined distance between the RP thin window and the silicon sensors, the alignment between the sensors and the beam has an uncertainty of 200 μm. FIXME: CHECK NUMBER

2. Relative track-based alignment: Individual detector planes in a detector package and in a unit are aligned with respect to each other using reconstructed tracks. The precision of the alignment procedure depends on the number of events collected and track distributions. Typical uncertainties obtained are few μm for the (X,Y) shifts, and less than 0.1 mrad for the rotation.

   need a sketch to show the overlap of the new horizontal detectors with the verticals.

3. Alignment using elastic events: The global misalignment modes (e.g. common shifts or rotations of the entire unit with respect to the beam) are inaccessible to the track-based techniques but can be constrained by exploiting known symmetries of certain physics processes. A prominent example is the hit distribution in the vertical detectors of elastic scattering events that allows, once the optics has been properly understood, to consider the two elastically scattered protons as an ideal ruler.

The RP station alignment based on the symmetry of the elastic scattering hit distribution is illustrated in Fig. 21. The left plot shows a distribution of track intercepts for vertical detectors in a detector plane in a RP station at 220 m. The tilt of the vertical band is mainly caused by optics imperfections. The center plot shows the vertical alignment. Data that might be affected by acceptance effects (gray bands) are removed from the vertical hit distributions. The symmetry line of the vertical distribution is the position of the beam center (black dash-dotted line) and is obtained by inverting the sign of the $y < 0$ distribution (blue), and shifting it until it coincides with the $y > 0$ part (red). Finally, the horizontal alignment and
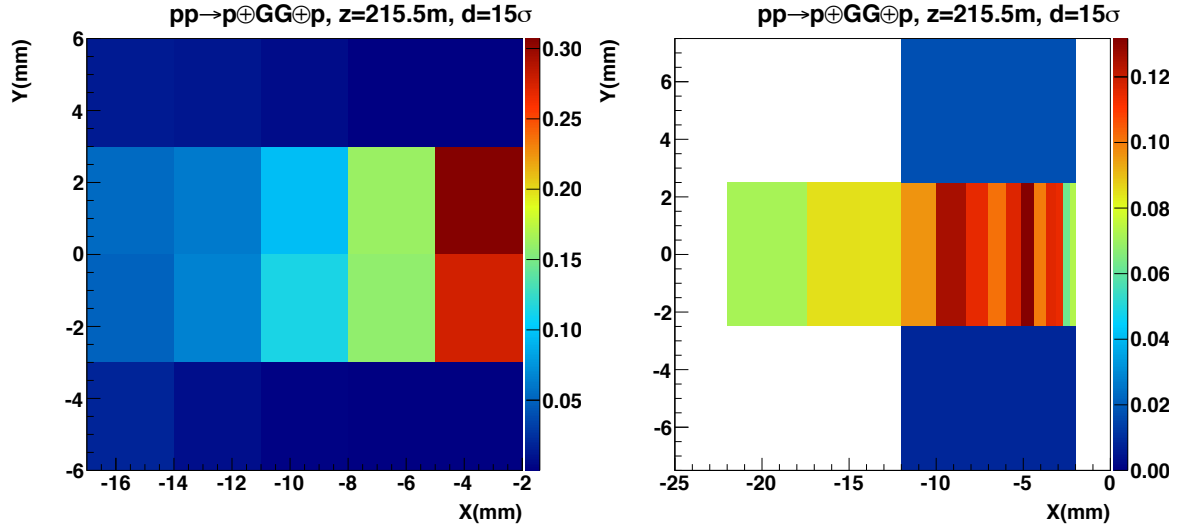
Figure 18: Detector occupancy of the time-of-flight detectors (at z=215.5 m) at 15σ from the beam center, with a segmentation corresponding to QUARTIC (left) or "diamond-like" (right) geometries. Smearing effects due to vertex position, beam energy dispersion and crossing angle are accounted for. Particles with the ExHuME signal generator to simulate exclusive dijet events, and 50 pileup interactions are superimposed on the primary interaction.

the unit rotation are established by fitting the track distribution, as shown in the right plot. A discussion of the alignment methods is detailed in Ref. [46].

The final alignment with elastic scattering has worked reliably for the TOTEM runs at low luminosity. If this method can be used at high luminosity has to be tested at the beginning of Run II. If we assume to insert the TOTEM vertical RP at 13σ from the beam, the smallest t observable would be 4.5 GeV^2. The visible cross section ranges, depending on the model used, between $3 \cdot 10^{-8}$ and $1 \cdot 10^{-6}$. With an instantaneous luminosity of $\sim 10^{34} cm^{-2} Hz$, the observable elastic rate is between 0.3 and 10 Hz, allowing the collection of 1k-36k event/h which are sufficient to perform the alignment and get a resolution of the order of 10μm.

should we comment about the radiation on vertical detectors?

An alternative method developed to dynamically determine the alignment of the CDF Roman Pot Spectrometer at the Tevatron during the data collection period is also briefly described below. This is a self-consistent data-driven method, and it uses an *in-situ* calibration to perform the alignment. It uses the fact that in the proximity of $t = 0$, the t-distribution can be represented by an exponential form, $d\sigma/dt = Ne^{-bt}$, where N is an arbitrary normalization factor and b the slope of the distribution. Alignment is achieved by seeking a maximum of the $d\sigma/dt$ distribution at $t = 0$. The implementation of the alignment method consists of introducing software offsets in the X and Y coordinates of the tracking detectors with respect to the physical beamline position, and iteratively adjusting them until a maximum for $d\sigma/dt$ at $t = 0$ (or of the dominant slope b) is found at the (X, Y) position where the tracking detector is correctly aligned. This method is limited by the size of the data sample and the variations of the beam position during data taking. The method is discussed in detail in Ref. [49].

2.8 Physics processes

Study of physics processes with forward protons may extend the physics reach of the LHC experiments. Here, we study two physics cases which address different issues: exclusive dijet and exclusive WW production. These processes will allow us to investigate central exclusive production with both protons
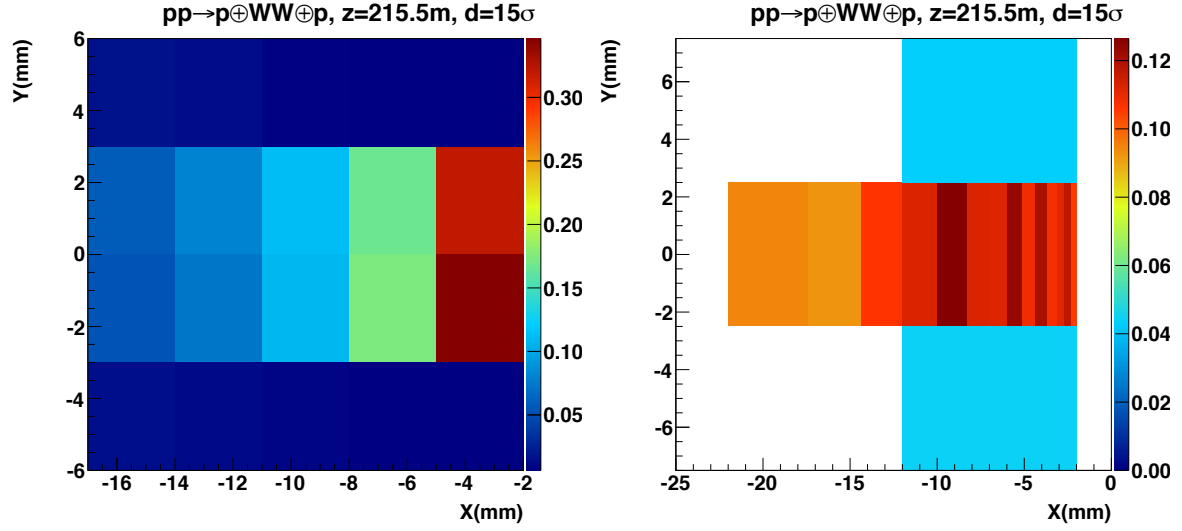
Figure 19: Detector occupancy of the time-of-flight detectors (at z=215.5 m) at 15σ from the beam center, with a segmentation corresponding to QUARTIC (left) or "diamond-like" (right) geometries. Smearing effects due to vertex position, beam energy dispersion and crossing angle are accounted for. Particles with the FPMC signal generator to simulate exclusive WW events, and 50 pileup interactions are superimposed on the primary interaction.

measured in the mass region above 200 GeV, as well as to learn about rates, backgrounds, and operational aspects of the forward detectors. Knowledge already gained in operating the TOTEM experiment during Run 1, and the experience of combined CMS-TOTEM data-taking will be used. The exclusive dijets produced in gluon-gluon fusion will allow to test the theory of exclusive QCD physics. These jets are predicted to be nearly 100% gluon jets with a small admixture of $b\bar{b}$. The more rare high-energy two-photon exclusive production of $\gamma\gamma \to WW$ will extend the possibility to study quartic gauge-couplings as well as to study deviations from the expected $\gamma\gamma$ mass spectrum due to possible new BSM particle production. Schematic leading-order diagrams of these two processes are shown in Fig. 22.
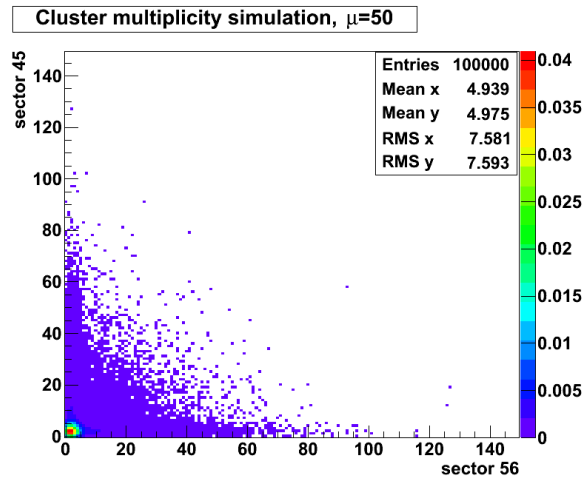

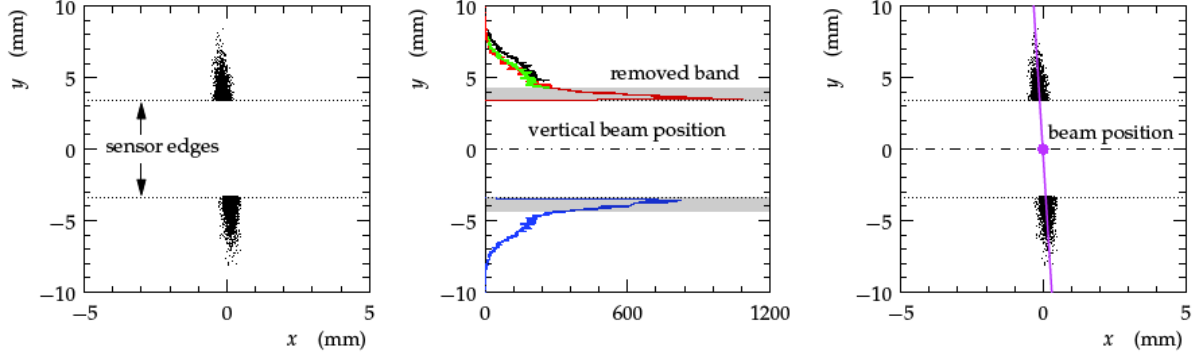Figure 20: Cluster multiplicity per bunch crossing at $\mu = 50$.

Figure 21: Alignment with selected elastic events. A selection of elastic events (*left:*); vertical alignment (*center*); horizontal alignment and the unit rotation are established by fitting the track distribution (*right*). The procedure is discussed in detail in the text.
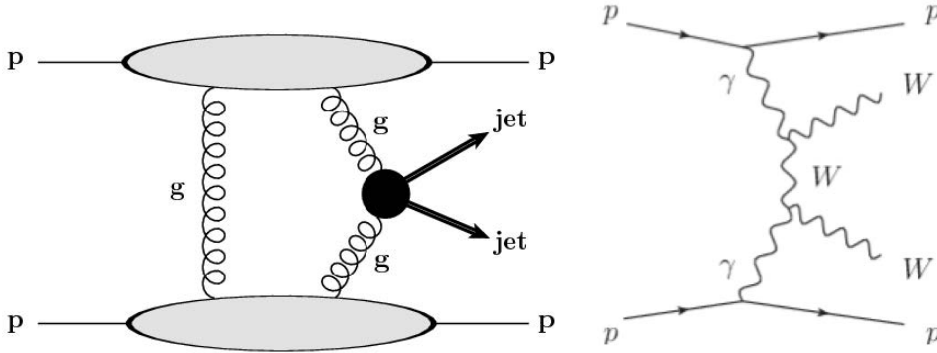

Figure 22: Leading order diagrams for exclusive dijet (left) and exclusive WW (right) production in pp collisions.

2.8.1 Central exclusive dijet production

Exclusive dijet production in proton-proton collisions is a process in which both protons escape intact the hard interaction, and a two-jet system is centrally produced $pp \rightarrow p' JJ p'$. This process is a particular case of dijet production in Double Pomeron Exchange (DPE), a diffractive process in which the protons suffer a small fractional momentum loss, and a system X containing two jets is produced, $pp \rightarrow (p'\mathbb{P})(p'\mathbb{P}) \rightarrow p'Xp'$. The Pomeron $\mathbb{P}$ is an exchange consisting of a colorless combination of gluons and/or quarks carrying the quantum numbers of the vacuum. Dijet production in DPE is a sub-process to dijet production in single-diffraction (SD) dissociation, where only one proton survives while the other dissociates. A schematic diagram for DPE dijet production is shown in Fig. 22 (left). Dijet production in DPE may occur as an exclusive process with only the jets in the final state, and no Pomeron remnants. In a special case, exclusive dijets may be produced through an intermediate state of a Higgs boson decaying into $b\bar{b}$. Exclusive production may also occur through a t-channel two-gluon exchange at leading order in perturbative QCD as shown schematically in Fig. 22 (left).

Exclusive dijet production was first observed at the Tevatron [48] in hadronic collisions. A first study of dijet production at $\sqrt{s} = 7$ TeV is presented in Ref. [50]. Here, a sensitivity reach of a study of high-p_T exclusive dijet events is investigated. In addition to providing information on QCD aspects of vacuum quantum number exchange, there is currently intense interest in using measured exclusive dijet production cross sections to calibrate theoretical predictions for exclusive Higgs boson production at the LHC. Such predictions are generally hampered by large uncertainties due to non-perturbative suppression effects associated with the rapidity gap survival probability. As these effects are common to exclusive dijet and Higgs boson production mechanisms, dijet production potentially provides a standard candle

process against which to calibrate the theoretical models. Furthermore, any centrally produced system of mass X may appear as an excess over background expectations. With the addition of the PPS as "proton taggers", a significant enhancement of the sensitivity to these physics processes may be reached.

The current study is based on the experimental techniques developed in Ref. [48, 50], and it is intended to explore the sensitivity reach of when the PPS detector is used. A sample of exclusive dijet events is used to study the $pp \rightarrow pJJp$ process, in which both forward protons are detected in the PPS.

The t-distribution of the exclusive dijet sample before any event selection is shown in Fig. 23 for signal and for pileup events, separately.

At the trigger level, events are selected by requiring at least two jets with uncorrected transverse momentum larger than xx GeV. Offline, events are selected by requiring a time coincidence in both arms of the PPS. Leading protons are in the PPS fiducial region, and the time-of-flight difference of their arrival at the PPS location is required to be less than 10 ps (30 ps), comparable to the expected detector resolution. Two reconstructed jets with corrected transverse momenta $p_T > 50$ GeV in the central detector ($\eta < 2.0$) are also required. Finally, a correction due to the instrumental background from additional sources (Sec. 2.6) is applied. FIXME: ADD RESULTS FOR 30PS, AND ETA COVERAGE UP TO 2.4 Backgrounds to this study come from minimum bias events, including elastic or single diffractive events, in coincidence with either two jets in the central detector or another leading proton within the PPS detector acceptance. FIXME: BKGS TO BE INCLUDED (OR NOT TO BE EXCLUDED) The event yields, relative cumulative efficiency, and resulting cross section values summarized in Tab. 3 are normalized to an integrated luminosity of 1 fb^{-1}.
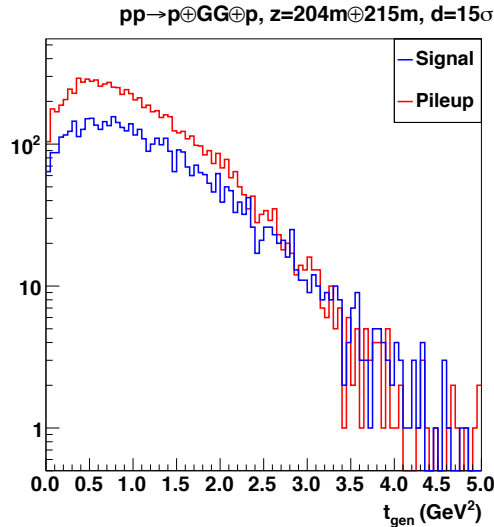

Figure 23: FIXME: DISTRIBUTION TO BE CHECKED t-distribution for signal and pileup events in the exclusive dijet sample. Coincidence of hits in the tracking stations at z=204 m and z=215 m (on one side of the IP) is required. Tracking detectors are located at a distance of 15 σ from the beam center. Smearing effects due to vertex position, beam energy dispersion and crossing angle are accounted for. Particles with the ExHuME signal generator to simulate exclusive dijet events, and 50 pileup interactions are superimposed on the primary interaction.

2.8.2 Central exclusive WW production

Study of high-energy photon interactions at the LHC opens up the possibility of interesting and novel research [51, 52]. In particular, measurements of the two-photon production of a pair of W-bosons provide sensitivity to anomalous quartic gauge couplings of the gauge bosons. Measurements of the exclusive

26

Table 3: TABLE TO BE UPDATED Number of expected signal events, relative cumulative efficiency, and cross section times branching fraction ($\sigma \times \mathcal{B}$) after each selection cut, for a sample of exclusive dijet events. Yields are normalized to an integrated luminosity of 1 fb^{-1}. Pileup events are included. Statistical uncertainties are shown.

Selection	Events	Relative cumulative efficiency	$\sigma \times \mathcal{B}$ (fb)
total number of events	1700±xx	100%	xx
PPS tagging ($\Delta t \leq 10$ps)	87± xx	5.1%	xx
at least 2 jets ($p_T > 50$ GeV)	52± xx	3.1%	xx
$\eta(\text{jet1}) < 2.0, \eta(\text{jet2}) < 2.0$	50± xx	2.9%	xx
no overlapping hits in timing detectors	xx± xx	xx%	xx

two-photon production of muon and electron pairs, in the process $pp \rightarrow p\ell^+\ell^-p$, were performed using 5.05 fb^{-1} of data collected in proton-proton collisions at $\sqrt{s} = 7$ TeV with the CMS detector at the LHC in 2011 [53]. Model-independent upper limits were extracted and compared to predictions involving anomalous quartic gauge couplings.

The current study is based on the experimental techniques developed in Ref. [53] and is intended to explore the potential sensitivity reach of the PPS detector. With the integrated luminosity expected to be collected during Run 2 and with the upgraded PPS detectors used in combination with the CMS central detector, the experimental reach can be extended by several orders of magnitude with respect to the best limits obtained so far.

In the process $pp \rightarrow pWWp$, both forward-scattered protons are detected in the PPS, depending on the acceptance of the mass of the WW central system produced (Fig. 15). Such a production process is characterized by a primary vertex from a $\ell^\pm\ell^\mp$ (where $\ell = e, \mu$) pair with no other track, a large transverse momentum of the dilepton system, $p_T(\ell^\pm\ell^\mp)$, and a large invariant mass, $M(\ell^\pm\ell^\mp)$.

A sample of exclusive $pp \rightarrow pWWp$ events is used, and only the $\mu\mu$ final state is selected. The dominant backgrounds come from inclusive W^+W^- and exclusive $\tau^+\tau^-$ pair production.

The simulated samples for the signal process are compared to the SM expectation for the backgrounds. Tails of the $p_T(\ell^\pm\ell^\mp)$ distribution, where the SM $\gamma\gamma \rightarrow W^+W^-$ contribution is expected to be small, are investigated to look for anomalous quartic gauge couplings.

Events are selected by requiring two leptons of opposite charge, with a minimum transverse momentum $p_T > 20$ GeV, above the trigger threshold. In order to reduce the contamination from the W+jet (or other non-prompt lepton) background, "tight" lepton identification criteria are required (as in Ref. [53]). Protons in the PPS detector acceptance are expected, and the presence of hits in both tracking and timing detectors is therefore required. Finally, a correction due to the instrumental background from additional sources (as discussed in Sec. 2.6) is applied. Table 4 summarizes the event yields after each selection cut, the relative cumulative efficiency, and the expected cross section (including the branching fraction). Yields are normalized to an integrated luminosity of 100 fb^{-1}.

After the full event selection, event yields for signal and background events are summarized in Tab. 5, for an integrated luminosity of 100 fb^{-1}.

Information of the proton time-of-flight arrival to the PPS detector location can be used as additional background rejection. After requiring coincidence of hits in both tracking and timing detector stations, the time-of-flight difference between the two leading protons arriving to the PPS detector location on opposite sides of the IP is shown in Fig. 24 as a function of the z-vertex position of the leading central

Table 4: Number of expected signal events, relative cumulative efficiency, and cross section times branching fraction ($\sigma \times \mathcal{B}$) after each selection cut, for a sample of exclusive WW events. Yields correspond to an integrated luminosity of 100 fb^{-1}. Only the $\mu\mu$ final state is considered. Statistical uncertainties are shown.

Selection	Events	Relative cumulative efficiency	$\sigma \times \mathcal{B}$ (fb)
generated $\sigma \times \mathcal{B}(WW \to \mu\mu)$	43± xx	100%	0.43±0.01
≥ 2 muons ($p_T > 20$ GeV, $\eta < 2.4$)	26± xx	61%	0.26±0.01
opposite charge muons, "tight" identification	23± xx	53%	0.23±0.01
protons in PPS detectors (timing and tracking)	5± xx	12%	0.051±0.003
no overlapping hits in timing detectors	3± xx	8%	0.033±0.003

Table 5: FIXME: PRELIMINARY, TO BE CHECKED Yields for signal and background events after the full event selection. Yields correspond to an integrated luminosity of 100 fb^{-1}. Only the $\mu\mu$ final state is considered. Statistical uncertainties are shown.

process	events
exclusive WW events (signal)	3.3± xx
inclusive WW + pileup	230± xx
exclusive $\tau\tau$ events	0.3± xx

muon for signal and background events. Here, background includes inclusive WW events in coincidence with pileup events. Distributions corresponding to timing resolutions of 10 ps and 30 ps are shown for signal and background events.
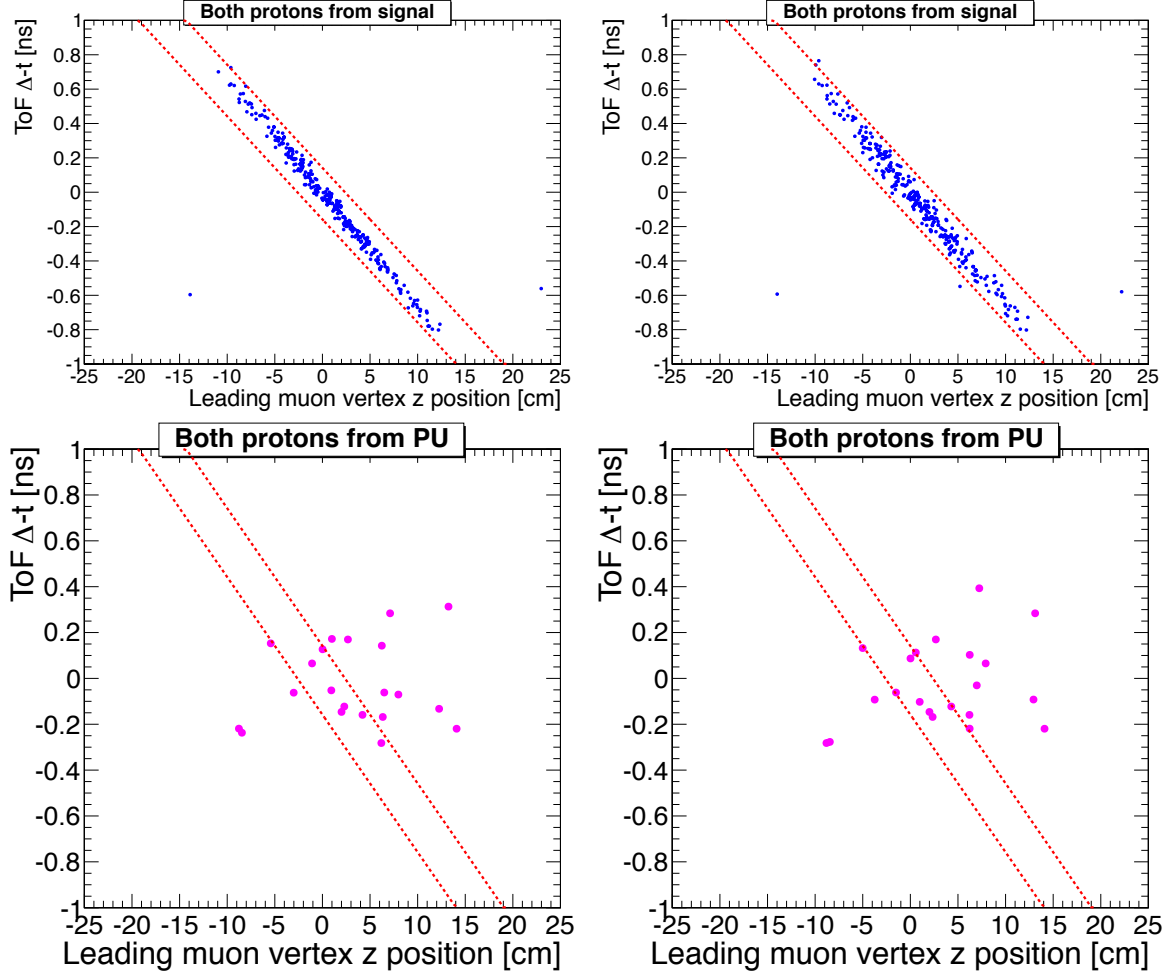

Figure 24: Time-of-flight difference between the two leading protons arriving to the PPS detector location on opposite sides of the IP as a function of the z-vertex position of the leading central muon for signal (top) and background inclusive WW (bottom) events. Timing resolutions of 10 ps (left) and 30 ps (right) are assumed. Distributions are shown after the full event selection. The dotted lines show an ideal window that retains close to 100% of signal events (for 30 ps resolution).

Kinematic distributions after the full event selections are shown in Fig. 25. The transverse momentum of the dimuon system, the azimuthal angle difference between the two leading muons, and the missing mass distributions are shown for signal and for the background exclusive $\tau\tau$ events. The missing mass $M_X = \sqrt{s\xi_1\xi_2}$ is estimated from the values of the two leading protons, ξ_1 and ξ_2. Background events are multiplied by a factor of FIXME: xx in order to allow comparison of the shapes.

Missing: - trigger: need to estimate the rates and trigger strategy for the processes described?
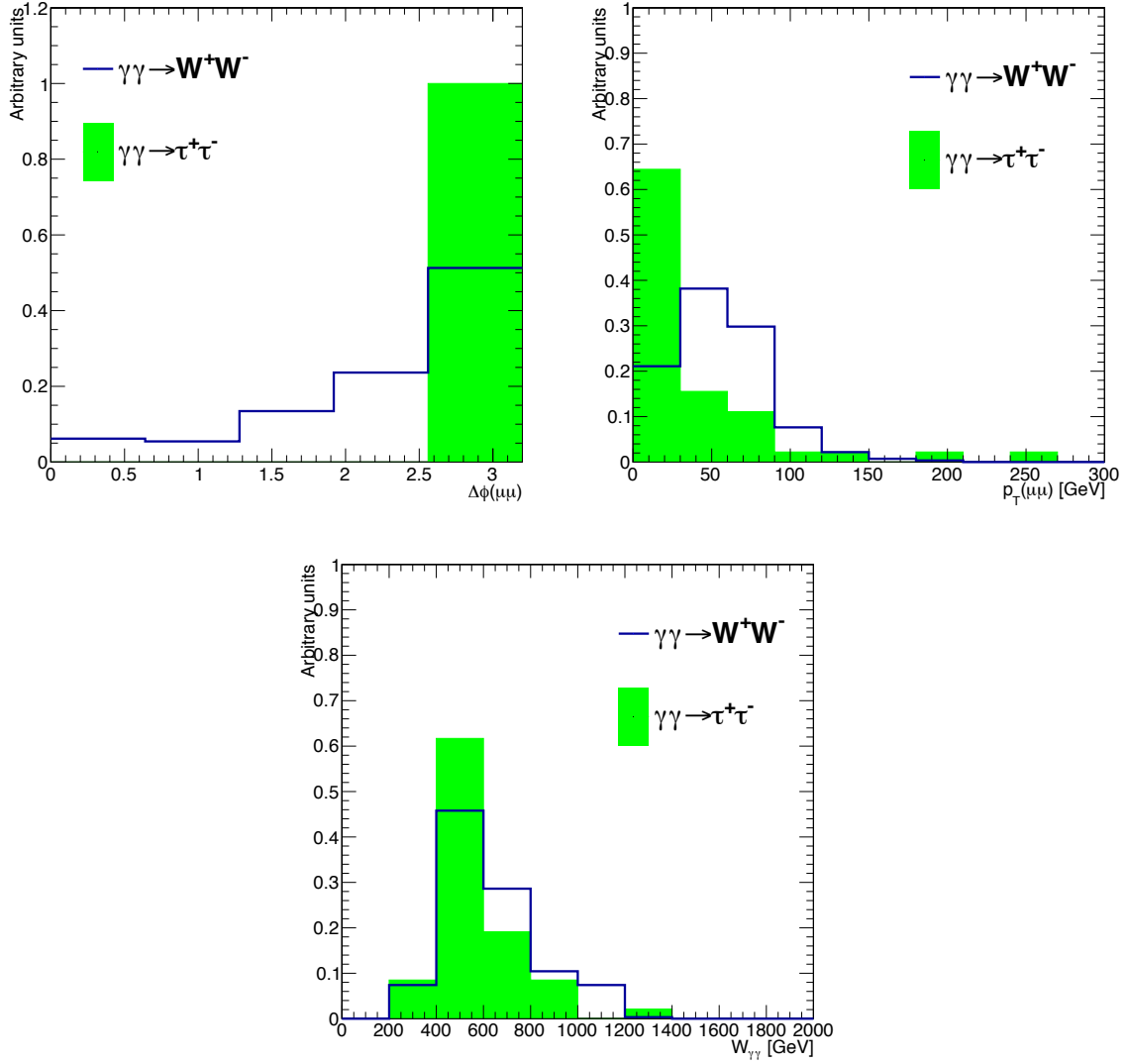
Figure 25: FIXME: FIX PLOTS Azimuthal angle difference between the two leading muons (top, left), transverse momentum of the di-muon pair (top, right), missing mass (bottom) for signal and background events. Distributions are shown after the full event selection. Yields of the background events are multiplied by a factor of FIXME: xx.